FULL PAPER

V_2O_5 Nano-Electrodes with High Power and Energy Densities for Thin Film Li-Ion Batteries

*Yanyi Liu, Michael Clark, Qifeng Zhang, Danmei Yu, Dawei Liu, Jun Liu, and Guozhong Cao**

Nanostructured V_2O_5 thin films have been prepared by means of cathodic deposition from an aqueous solution made from V_2O_5 and H_2O_2 directly on fluorine-doped tin oxide coated (FTO) glasses followed by annealing at 500°C in air, and studied as film electrodes for lithium ion batteries. XPS results show that the as-deposited films contained 15% V^{4+}, however after annealing all the vanadium is oxidized to V^{5+}. The crystallinity, surface morphology, and microstructures of the films have been investigated by means of XRD, SEM, and AFM. The V_2O_5 thin film electrodes show excellent electrochemical properties as cathodes for lithium ion intercalation: a high initial discharge capacity of 402 mA h g^{-1} and 240 mA h g^{-1} is retained after over 200 cycles with a discharging rate of 200 mA g^{-1} (1.3 C). The specific energy density is calculated as 900 W h kg^{-1} for the 1st cycle and 723 W h kg^{-1} for the 180th cycle when the films are tested at 200 mA g^{-1} (1.3 C). When discharge/charge is carried out at a high current density of 10.5 A g^{-1} (70 C), the thin film electrodes retain a good discharge capacity of 120 mA h g^{-1}, and the specific power density is over 28 kW kg^{-1}.

1. Introduction

Energy storage technology is incontrovertibly one of the great challenges in a modern society that faces environmental and ecological concerns. Lithium ion batteries are regarded as one of the most important energy storage technologies due to their extensive applications in a wide range of areas including portable electronic devices, electric vehicles, and implantable medical devices. [1,2] As energy storage materials are the heart of clean energy devices, the development of new and improved materials are key to the production of a new generation of such devices for the 21st century. Nanostructured materials are attracting increasing interest in the field of energy materials due to the superior electrochemical properties resulting from their nanoscale dimensions, high surface area, and large structural freedom. Such materials could provide high energy and power density while maintaining mechanical integrity and chemical stability over many intercalation/deintercalation cycles.[3–6]

Vanadium oxide is an attractive multifunctional material possessing extensive applications in various fields.[7–21] Since its first investigation as a battery material for lithium ion batteries over 40 years ago,[22] it has been discovered that during Li^+ ion intercalation, vanadium pentoxide (V_2O_5) possesses high specific electrochemical capacity (theoretical capacity 450 mA h g^{-1}) with four phase transitions involving five successive phases of $Li_xV_2O_5$ ($0 < x < 3$): α ($x < 0.01$), ε ($0.35 < x < 0.7$), δ ($0.9 < x \leq 1$), γ ($0 < x \leq 2$), and the irreversible ω ($x > 2$).[15,23–24] Although the Li-ion intercalation voltage is lower than for $LiCoO_2$ or $LiMn_2O_4$, V_2O_5 is still regarded as one of the most popular cathode candidates for Li ion batteries both in academia and industry due to the following advantages: i) V_2O_5 provides higher energy and power density than $LiCoO_2$ and $LiFePO_4$,[25,26] ii) it has an easier and more controllable fabrication method than $LiMO_2$ (M = Ni, Mn, Co, Fe),[27,28] and iii) it has a higher capacity and better cyclic stability than $LiMn_2O_4$.[29,30] Various processing methods to prepare nanostructured vanadium pentoxide with the high electrochemical performance required for lithium ion batteries exist: self-assembly of V_2O_5 hollow microspheres from nanorods;[16] V_2O_5 sub-microbelt fabrication from sol-gel precursors combined with a hydrothermal method; [17] Electrospinning of V_2O_5 nanofibers;[18,31] Electrostatic spray-deposition of V_2O_5;[32] co-precipitation of V_2O_5 macro-plates from water/ethanol media;[33] and deposition of V_2O_5 nanowires from chemical vapor transport.[34] These nanostructured vanadium pentoxide materials have shown much improved electrochemical performance in comparison with conventional cathode materials for lithium ion batteries,[34,35] however due to the high cost of fabrication and complicated processing methods, the broad

Y. Y. Liu, M. Clark, Dr. Q. Zhang, Prof. D. Yu, Dr. D. Liu, Prof. G. Cao
Department of Materials Science and Engineering
University of Washington
Seattle, WA 98195, USA
E-mail: gzcao@u.washington.edu
M. Clark
Department of Physics and Astronomy
University of British Columbia
Vancouver V6T 1Z1, Canada
Prof. D. Liu
College of Chemistry and Chemical Engineering
Chongqing University
Chongqing 400044, P.R. China
Dr. J. Liu
Pacific Northwest National Laboratory
902 Battelle Boulevard
P.O.Box 999, Richland, WA 99352, USA

DOI: 10.1002/aenm.201000037

industrial applications of such nanomaterials are limited. In this research, for the first time we reported a simple, low-cost cathodic deposition method for producing nanostructured V_2O_5 thin films from a solution of V_2O_5 and H_2O_2. Such deposited films possess unique nanostructure, which could facilitate the phase transition during Li^+ insertion, therefore achieving high energy and power density with excellent cyclic stability when tested as thin film cathode for Li-ion batteries. The film formation mechanism, crystallinity phase, morphology, and electrochemical properties were investigated and discussed.

2. Results and Discussions

2.1. Film Preparation

After mixing of V_2O_5 powders and an excess of H_2O_2 with deionized (DI) water (specific compositions are noted in the Experimental Section), the resulting yellow slurry bubbled vigorously, which was accompanied with slight color change to orange (note that this reaction is exothermic). Several parallel or sequential chemical reactions occur in association with the decomposition of excess H_2O_2, as detailed in the literature: [36,37]

$$V_2O_5+4H_2O_2 \rightarrow 2[VO(O_2)_2(OH_2)] - +2H^+ + H_2O \quad (1)$$

$$V_2O_5+2H^+ +2H_2O_2+3H_2O \rightarrow 2[VO(O_2)(OH_2)_3]^+ + O_2 \quad (2)$$

$$2[VO(O_2)_2(OH_2)]^- +4H^+ +2H_2O \rightarrow 2[VO(O_2)(OH_2)_3]^+ +O_2 \quad (3)$$

$$2[VO(O_2)(OH_2)_3]^+ \rightarrow 2[VO_2]^+ +O_2+6H_2O \quad (4)$$

$$[VO2]^+ \rightarrow \text{gelation} \quad (5)$$

The color change could be ascribed to the formation of diperoxovanadate anion $[VO(O_2)_2(OH_2)]^-$ (Equation 1).[38] After 5 min the slurry transformed into a transparent ruby red solution, which suggests that the main ion species in the solution is the red monperoxovanadate cation $[VO(O_2)(OH_2)_3]^+$ (Equations 2 and 3).[39] After adding more DI water to dilute the solution to 0.06 M, the solution was sonicated for an hour and gradually turned to a brownish red solution with a higher viscosity. This change can be ascribed to the transformation of the ion species into the dioxovanadium cation $[VO_2]^+$ (Equation 4).[37,40] It should be noted that the vigorous bubbling observed during the mixing of V_2O_5 and H_2O_2 is the result of the release of oxygen gas from Equations 3 and 4; each V_2O_5 releases 2 O_2. The increased viscosity and formation of the brownish red gel suggests the beginning of $V_2O_5 \cdot nH_2O$ gelation (Equation 5).[37,41]

After sonication, the brownish red mixture of $V_2O_5 \cdot nH_2O$ gel and solution was diluted to 0.0075 M with pH = 2.7 for the deposition. During cathodic deposition, electrons move toward the negative side, therefore the V^{5+} species from V_2O_5 colloidal particles and the dioxovanadate cations VO_2^+ are reduced on the surface of the FTO glass (Equation 6–7):

$$V_2O_5+4H^+ \leftrightarrow 2VO_2^+ +2H_2O \quad (6)$$

$$VO_2^+ +e^- \rightarrow VO_2 \quad (7)$$

Upon deposition of VO_2 on the FTO substrate surface, VO_2 (with V^{4+}) serves as a nucleation center that initiates and catalyzes the formation of $V_2O_5 \cdot nH_2O$ through low pH conditions. [12,36,42–49]

$$2[VO_2]^+ +nH_2O \rightarrow V_2O_5 \cdot nH_2O + 2H^+ \quad (8)$$

Consequently, hydrous vanadium oxide is deposited through a combination of parallel yet sequential cathodic depositions and catalyzed gelation. It should be noted that gelation (Equation 8) without the V^{4+} catalyst typically takes more than 24 h.

In spite of the fact that above chemical reactions have been well studied and documented,[36,37] the present study is the first effort, to the best knowledge of the authors, to deposit films through the combination of the cathodic deposition of VO_2 and V^{4+}-catalyzed gelation, forming a mixed thin film of VO_2 and $V_2O_5 \cdot nH_2O$ deposited on an FTO glass substrate to be directly applied as cathodes for thin film Li-ion batteries. Although other deposition methods have been studied for the formation of V_2O_5 films, cathodic deposition is unique as V^{5+} is simultaneously reduced to V^{4+} during film fabrication. Consequently the V_2O_5 films contain a significant amount of V^{4+} ions, which serve three important functions: i) as nucleation centers for phase transition for film deposition, ii) as initiators for the sol-gel processing, and iii) as efficient catalysts for the formation and gelation of hydrous V_2O_5 films. The cathodic deposition of V_2O_5 thin films is low cost and easy to control, and thus could have fundamental significance in the commercial battery field, as it could lead to fabrication of binder-free and additive-free large-scale film batteries.

Figure 1 shows photographs of V_2O_5 films deposited on FTO glass substrates at –2.4 V after 3 min. Figure 1**a** compares the as-deposited $V_2O_{5-x} \cdot nH_2O$ film after drying in air for a day and the V_2O_5 films annealed at 500 °C; Figure 1**b** shows a V_2O_5 film prepared and annealed at 500 °C over a 1 inch × 1 inch in area with no detectable defects. The as-deposited films are green-yellow in color before heat treatment, rather than the yellow color often observed for V_2O_5 films or powders.[13] (VO_2 is known to be blue and V_2O_5 is yellow.)[50] The green-yellowish color observed in this study can be ascribed to a mix of yellow V^{5+} and blue V^{4+}, which was confirmed by XPS results (see below). For the sake of consistency and clarity, $V_2O_{5-x} \cdot nH_2O$ will be used to denote the films before heat treatment to differentiate from films with complete V^{5+} valence status after annealing at 500 °C.

Figure 2 shows the thickness of the film deposited at the negative side as a function of deposition time with a constant voltage of -2.4 V: curve (a) shows the deposition rate for the film before treatment, while curve (b) shows film thickness after annealing at 500 °C for 3 h. The deposition rates are 65 nm/min and 34 nm/min for the films before and after annealing, respectively. The noticeable reduction in film thickness after heat treatment corresponds to volume shrinkage and can be attributed to: i) the crystal structure change, and ii) partial densification. This is in good agreement with structural studies of $V_2O_5 \cdot nH_2O$ xerogels.[51–52] Both orthorhombic V_2O_5 and $V_2O_5 \cdot nH_2O$ xerogel have layered structures: the

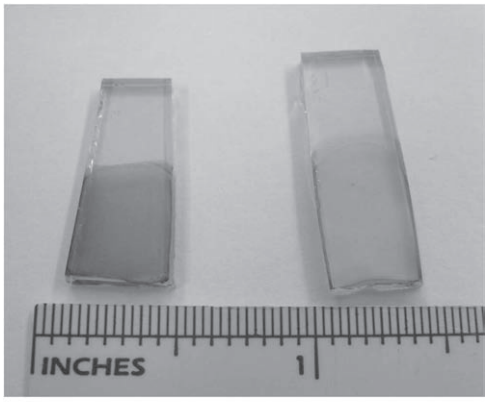

(a)

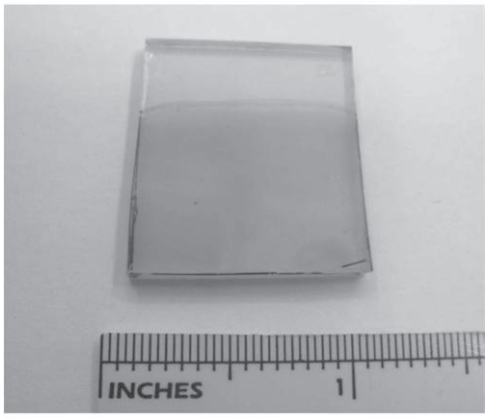

(b)

Figure 1. Photographs of the as-deposited $V_2O_{5-x}\cdot nH_2O$ films and 500 °C annealed V_2O_5 cathodse. a) The as-deposited $V_2O_{5-x}\cdot nH_2O$ film (left, green-yellow) and, the V_2O_5 film after annealing in air at 500 °C (right, yellow); b) Photograph of the 500 °C annealed V_2O_5 film, 1 inch×1 inch in area.

structure of orthorhombic V_2O_5 can be described by the packing of VO_5 square pyramids with a interlayer distance of ~ 4.5 Å along the *c*-axis of the orthorhombic cell,[15] while the structure of the $V_2O_5\cdot nH_2O$ xerogel is an assembly of bilayers of single V_2O_5 layers with VO_5 square pyramids with water molecules residing in between; the distance between each slab is 8 Å–21.6 Å depending on the crystalline water content in the $V_2O_5\cdot nH_2O$ xerogel.[51,52] V_2O_5 has a relatively low melting point and is often used as a sintering additive.[53,54] 500 °C is a relatively low annealing temperature for most oxides, but allows a noticeable densification of V_2O_5. Moreover, it can be observed that even with the drastic volume change after thermal treatment, the V_2O_5 films remained well affixed and stayed intact on the FTO glass substrate, without any macroscopic defects, cracks, or pin-holes. This was the case even for large-area films (1 inch by 1.5 inch in area, 500 nm in thickness). This can be ascribed to the good attachment between the films and the substrates induced by the external electrical field, as well as the fine, homogenous nanocrystallite (tens of nanometers in size) films formed by cathodic deposition from the V_2O_5 solution.

2.2. Film Characterization

In order to study the crystalline water loss during the annealing process, thermogravimetric analysis (TGA) was carried out in flowing air from 100 °C to 600 °C with a heating rate of 2 °C min^{-1} and the results are shown in **Figure 3**. It should be noted that since the $V_2O_{5-x}\cdot nH_2O$ films in this research contain V^{4+} species induced by cathodic deposition, the films will gain weight from oxidization when heated in air. However, the loss of the crystalline water will give a overall thermogravimetric trend of weight loss. Therefore, in this research, it is inaccurate to use the weight loss from TGA measurement to derive the quantity of crystalline water present. The TGA curve shows the thermogravimetric change happening over a different temperature range compared to other references, which is

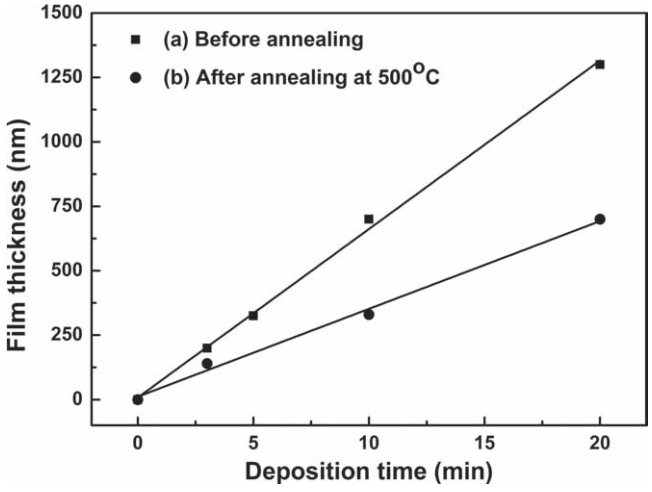

Figure 2. The relationship of deposition time and thickness of the a) as-deposited $V_2O_{5-x}\cdot nH_2O$ films and b) 500 °C annealed V_2O_5 films.

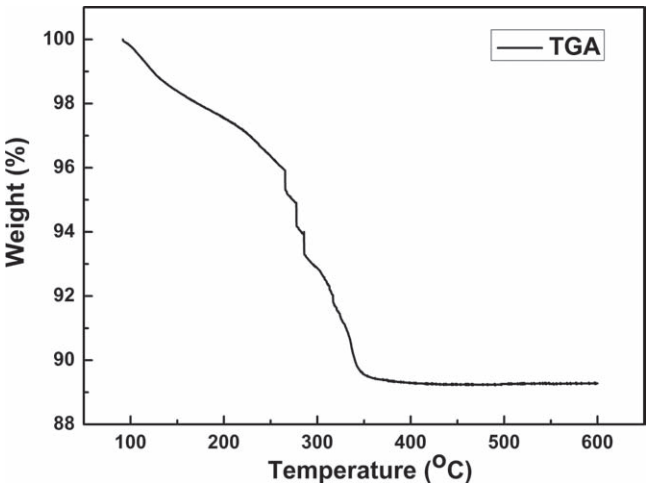

Figure 3. TGA curve of as-deposited $V_2O_{5-x}\cdot nH_2O$ film tested in the air from 100 °C to 600 °C with a heating rate of 2 °C min^{-1}.

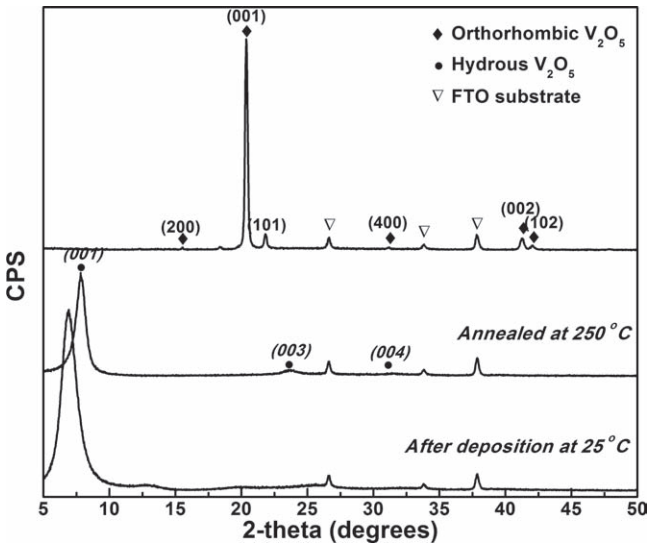

Figure 4. XRD patterns of the as-deposited $V_2O_{5-x}{\cdot}nH_2O$ film, hydrous $V_2O_{5-x}{\cdot}nH_2O$ films annealed at 250 °C and V_2O_5 films annealed at 500 °C in the air.

attributed to the various film-processing methods applied.[40,55–56] In this research the ~3% weight loss below 250 °C can mainly be ascribed to the loss of weakly bound water, and the weight loss between 250 °C and 340 °C generally involves the loss of crystalline water from $V_2O_{5-x}{\cdot}nH_2O$. Above 340 °C the crystallization of V_2O_5 occurs. This is consistent with the X-ray diffraction (XRD) results discussed in the following paragraphs.

Figure 4 compares the XRD patterns of the $V_2O_{5-x}{\cdot}nH_2O$ films after cathodic deposition from V_2O_5 at room temperature, and after annealing at 250, and 500 °C in air. The as-deposited film without any heat treatment shows an intense (001) peak, which indicates the characteristic layered structure of $V_2O_{5-z}{\cdot}nH_2O$. This is consistent with other research showing a preferential structure of ribbon stacking for $V_2O_5{\cdot}nH_2O$ gel.[13] The crystallite size calculated from the Scherrer Equation is 6.2nm, and the interlayer distance estimated from Bragg's law is 12.77 Å, which indicates the composition of crystalline water in this sample is $n > 2$.[14]

When heated to 250 °C, the improved crystallinity of the layered structural $V_2O_{5-x}{\cdot}nH_2O$ film was confirmed by the appearance of (003) and (004) peaks along with the (001) peak. It is seen that the (001) peak shifts to the higher angle direction, resulting in a decrease in the interlayer distance to 11.31 Å ($n \approx 1.5$)[57] due to the loss of crystalline water. The crystallite size grows slightly to 10.0 nm (calculated from the XRD pattern). The exhibition of a series of (00*l*) harmonics reflects the turbostratic nature of the stacking of V_2O_5 ribbons. Moreover, the missing peak corresponding to the (002) plane suggests the formation of double sheets of V_2O_5 for each layer.[58]

After the $V_2O_{5-x}{\cdot}nH_2O$ film was annealed at 500 °C, the sample was completely dehydrated, presenting a pure orthorhombic phase with good crystallinity, as shown in the XRD pattern. The interlayer distance along the *c*-axis is calculated as 4.36 Å, a perfect match with the crystalline structure of orthorhombic V_2O_5 (Joint Committee on Powder Diffraction Standards (JCPDS) No. 41–1426). The V_2O_5 films have a preferred orientation, evidenced by the missing diffraction pattern for (0*l*0) plane along the *b*-axis. The crystallization temperature of the orthorhombic phase at 500 °C, and of $V_2O_5{\cdot}1.5H_2O$ at 250 °C in this study is higher in comparison with other references.[14,51–52] The crystallite size of this orthorhombic V_2O_5 is calculated to be 35.1 nm from the XRD pattern.

X-ray photoelectron spectroscopy (XPS) measurements were carried out on the as-deposited $V_2O_{5-x}{\cdot}nH_2O$ films and the V_2O_5 films annealed in air at 500 °C to investigate the oxidation state of the vanadium as well as to estimate the content of reduced vanadium V^{4+} in the films. The V $2p_{3/2}$ core peak spectra for the as-deposited $V_2O_{5-x}{\cdot}nH_2O$ films (**Figure 5a**) is composed of two components located at 517.96 eV and 516.65 eV respectively, as shown in the fitting data. These two binding energy values can be associated with two formal oxidation degrees, +5

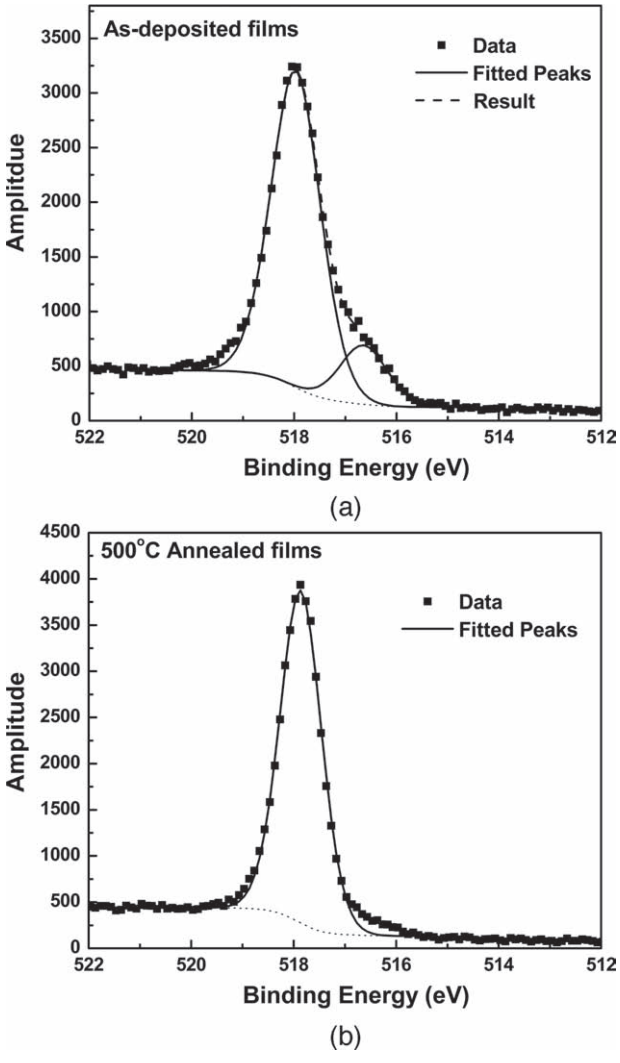

Figure 5. XPS spectrum of high-resolution scan on the V $2p_{3/2}$ core peaks performed on the films. a) The as-deposited $V_2O_{5-x}{\cdot}nH_2O$ films at room temperature. b) The V_2O_5 films after annealing at 500 °C in the air.

Table 1. Binding energy (E_B) of the V $2p_{2/3}$ core peaks taken from the spectrum in Figure 5.

Sample	V^{5+} peak area	V^{4+} peak area	V^{5+}/ V^{4+}	Binding Energy for V^{5+} (eV)	Binding Energy for V^{4+} (eV)
a	3523.41	635.13	85/15	517.96	516.65
b	3624.30	-	-	517.86	-

and +4.[59–62] However for the 500 °C annealed V_2O_5 films, there is only one V $2p_{3/2}$ core peak locating at 517.86 eV, as shown in Figure 5b, associated to the +5 formal degree for vanadium ions. This difference can be explained by the film preparation conditions: the as-deposited films form on the substrate placed on the negative side: some V^{5+} on the surface of the substrate becomes reduced to V^{4+}, which further catalyzed the gelation of the $V_2O_{5-x}\cdot nH_2O$ films.[12,36,42–49,63] Therefore, a noticeable V^{4+} concentration exists in the as-deposited films. After annealing at 500 °C in air, the introduction of oxygen leads to the oxidation and crystallization of the films and therefore the vanadium ions are present only in the highest oxidation degree (V^{5+}). The ratio of V^{4+}/V^{5+} is 15/85, which was derived from the area ratio of the fitted spectrum of V $2p_{3/2}$ (V^{5+}) and V $2p_{3/2}$ (V^{4+}), as listed in **Table 1**.[64,65] These results corroborate the film color observed in Figure 1a, and the cathodic deposition mechanism discussed in the film-preparation section.

Figure 6 a-d are scanning electron microscopy (SEM) images revealing the surface morphology and microstructures of the V_2O_5 films annealed at 500 °C for 3 h. The top views (Figure 6a and b) show that the uniform film was homogenously deposited, and composed of small "wrinkled" flakes (domain-like) of 0.5–1.5 μm diameter parallel to the substrate. Each flake is composed of smaller particles of 20–30 nm diameter, which agrees well with the crystallite size calculated from the XRD patterns. The cross-section view of the annealed V_2O_5 films (Figure 6c and d) shows similar nanostructures with 20–30 nm nanoparticles, and again agrees very well with the crystallite size calculated from the XRD patterns. 10 nm gaps separate the adjacent nanoparticles. It should be noted that the nanostructures and the size of the nanocrystallites remain the same at the surface and inside the film. It should also be noted that this nanostructure was not found in V_2O_5 thin films deposited on anodic substrates (Figure S1, Supporting Information).

The formation of such peculiar domain-nanocrystallite structured thin films may be explained by considering the fact that the film was deposited through a combination of cathodic deposition and catalyzed gelation. The formation of tetravalent vanadium ions or VO_2 by cathodic deposition initiates and catalyzes the gelation of hydrous vanadium pentoxide. Continued reduction and cathodic deposition of vanadium dioxide serves as a secondary (or new) nucleation, and consequently the deposited film consists of many nanoparticles stacking with spaces separating them from one another. The VO_2 particles could also be regarded as nucleation sites during the annealing process, which retards the nanocrystallite growth and suppresses the grain boundary migration (Figure 6c and d). The atomic force microscopy (AFM) image (**Figure 7**) of the surface of 500 °C annealed V_2O_5 thin films with an area of 4μm × 4μm shows that the flake size is about 0.5 μm×1.5 μm in the planar dimension, and the roughness of the film is measured to be +/–20 nm.

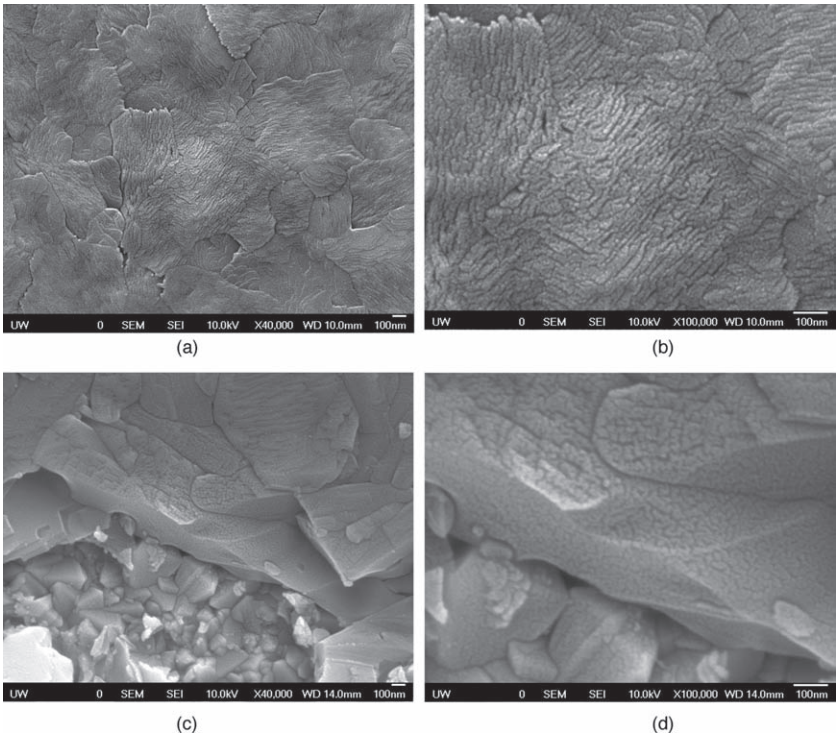

Figure 6. SEM image of the 500 °C annealed V_2O_5 film: a) top view, ×40 K, b) top view, ×100 K, c) cross-section view, ×40 K, d) cross-section view, ×100 K.

Figure 8 shows the 1st and 8th cycles of the cyclic voltammetry (CV) curves for 500 °C annealed V_2O_5 thin-film electrodes with thickness between 150–170 nm. It can be clearly observed that there are four cathodic peaks located at –0.192, –0.404, –1.320, and –1.797 V, and these four peaks correspond to the α/ε, ε/δ, δ/γ, γ/ω phase transitions within the potential range 0.6 V–-1.8 V (*Vs.* Ag^+/Ag), according to the literature. [23,24,65] The two anodic peaks at -0.096 V and -0.175 V can be ascribed to the reverse phase transitions of ε/α and δ/ε, which still leaves a broad peak after 8 cycles. [16,24] This is different from other studies, which show that when there is more than 2.2 mol Li^+ being intercalated into $Li_xV_2O_5$ ($x \geq 2.2$), especially at high current densities, an irreversible phase transition will occur, which results in a capacity loss due to kinetic limitations. [15,17,18,23,24,66] However in this research, we were able to observe partially reversible α/ε, ε/δ phase transitions at a current density of 200 mA g^{-1} (1.3 C) after 8 cycles. This is a proof of the facilitated thermodynamics and kinetics of the phase transition, which can be ascribed to the "wrinkled" nanostructure (Figure 6).

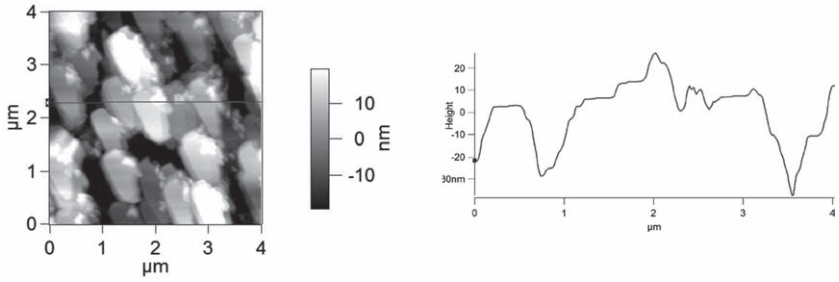

Figure 7. Surface morphology of the films annealed at 500 °C measured by AFM on 4 μm×4 μm area and surface roughness distribution along the red line as shown.

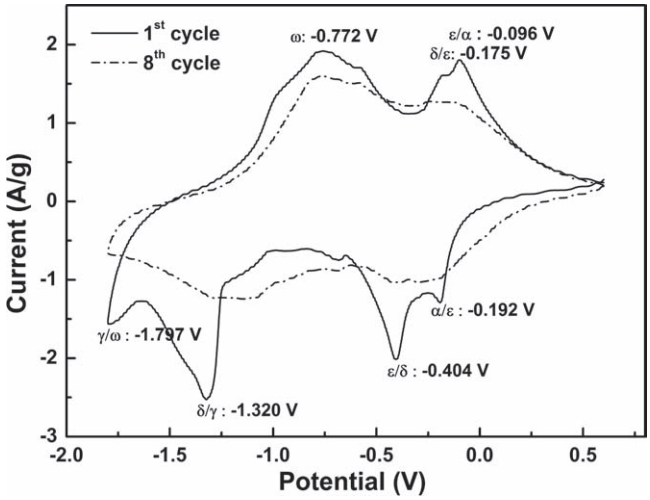

Figure 8. The cyclic voltammograms of 500 °C annealed V_2O_5 films with a scan rate of 5 mV s^{-1} in 1 M $LiClO_4$/PC electrolyte solution for the 1st cycle (solid line) and 8th cycle (dash-dot line)

The phase transition during lithium ion intercalation/deintercalation is made more favorable by the nanoscale dimensions as well as the accessibility of the intercalation sites. Nanostructured materials possess huge surface area and excessive surface energy, and thus offer more sites for lithium ion insertion and extraction and allow phase transitions that are otherwise difficult to achieve in bulk materials. The broad peak at –0.772 V that appears during anodic scanning is in good agreement with the irreversible formation of the ω phase,[24] further proved by the chronopotentiometric curves (**Figure 9**).

Figure 9 shows the chronopotentiometric (CP) curves for the first discharge/charge and second discharge curves of 500 °C annealed V_2O_5 thin film electrodes at a current density of 200 mA/g (1.3 C) in the potential range -1.6–0.2 V (*Vs.* Ag^+/Ag). The initial discharge curve presents four noticeable plateaus: –0.16, –0.34, –1.25, and –1.55 V, which correspond to the successive appearance of the following two-phase regions: α/ε, ε/δ, δ/γ, and γ/ω, with Li composition for $Li_xV_2O_5$ in a range of $0 < x \leq 2.68$ (related with a capacity of 402 mA h g^{-1}).[23,65] It can be observed that the first charge and second discharge curves maintain noticeable but shorter plateaus at the same potential positions, which are related to the above-listed phase transitions. These plateaus solidly prove the enhanced reversibility of phase transitions when more than 2 mols of Li^+ ions are inserted into theV_2O_5 films. Moreover it is noteworthy that, in the first discharge curve, the vertical drop connecting the two plateaus related to the ε/δ, δ/γ phase transitions becomes a slope in the successive first charge and second discharge curves. This sloped curve is rather similar to solid solution behavior, [24] which can be related to the formation of a new phase: ω-$Li_xV_2O_5$ ($x > 2$) and it is reported to be irreversible.[24,65] After the first charge 0.68 mol Li^+ was trapped in the newly formed ω phase; however the second discharge achieves a complete intake of Li^+ to form ω-$Li_{2.68}V_2O_5$. These CP curves are in good agreement with the CV results (Figure 8) in explaining the phase transitions of V_2O_5 films.

The cyclic performance of the V_2O_5 thin film electrodes annealed at 500 °C was investigated. **Figure 10** shows the discharge capacity at a current density of 200 mA g^{-1} (1.3 C) for the first 12 cycles, followed by 170 cycles of discharge/charge tests at various current densities (further discussed in **Figure 11**). The last 20 cycles, returned to a current density of 200 mA g^{-1} (1.3 C) for capacity fading investigations, are also shown in Figure 10. The initial discharge capacity is 402 mA h g^{-1}, which is related to $Li_{2.68}V_2O_5$ before the second charge begins. Due to the irreversible phase formation from the first charge, the second discharge capacity dropped to 368 mA h g^{-1}, and stayed at 325 mA h g^{-1} for the 12th cycle. The coulombic efficiency is 74.6% for the first cycle and 85.8% for the second cycle. After more than 180 cycles tested at different current densities, the discharge capacity was still as high as 240 mA h g^{-1}. The specific energy densities were calculated to be 900 W h kg^{-1} for the 1st cycle and 723 W h kg^{-1} for the 180th cycle when discharged at 200 mA g^{-1} (1.3 C). These values are higher than the data previously reported for V_2O_5 cathode materials in lithium ion batteries.[16,18–19,23,32,67–69] Figure 11 shows the cyclic discharge capacity of 500 °C annealed

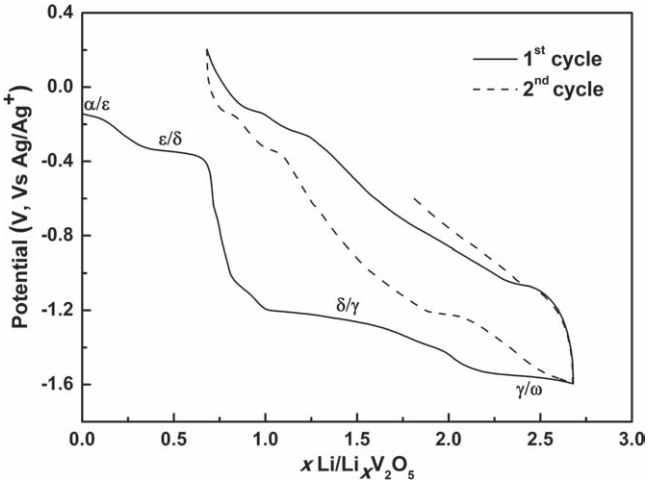

Figure 9. Chronopotentiometric curves for the first discharge/charge and second discharge cycles of 500 °C annealed V_2O_5 thin film cathodes at a current density of 200 mA g^{-1} (1.3 C) in the potential range of –1.6 V–0.2 V (*Vs.* Ag^+/Ag).

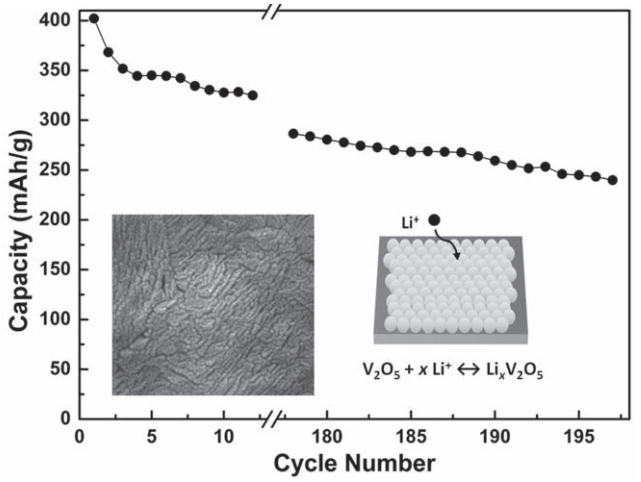

Figure 10. The cyclic performance of 500 °C annealed V_2O_5 thin film cathodes at a current density of 200 mA g^{-1} (1.3 C). (Inset shows the SEM image of the V_2O_5 film surface, and a schematic drawing of the enhanced Li^+ diffusion in the unique nanostructured V_2O_5 film with its high surface area and short difussion path)

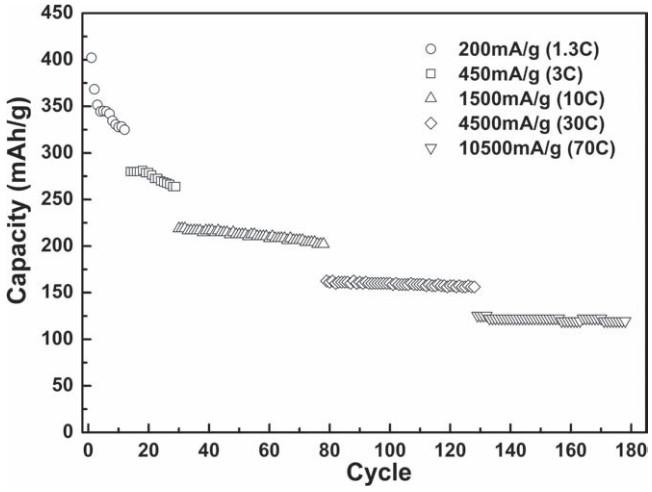

Figure 11. The cyclic performance of 500 °C annealed V_2O_5 thin film cathodes at various current densities from 200 mA g^{-1} (1.3 C) to 12.5 A g^{-1} (70 C) for up to 177 cycles.

V_2O_5 films performed at various current densities at 200 mA g^{-1} (1.3 C), 450 mA g^{-1} (3 C), 1.5 A g^{-1} (10 C), 4.5 A g^{-1} (30 C) and 10.5 A g^{-1} (70 C). At fairly high current densities, which correspond to fast battery discharge/charge cycles, the film electrode retains a high lithium ion storage capacity: 160 mA h g^{-1} at 4.5 A g^{-1} (30 C) and 120 mA h g^{-1} at 10.5 A g^{-1} (70 C), or with a high specific power of 28 kW kg^{-1}.

The cathodic deposited V_2O_5 thin film electrodes from this research show much higher lithium intercalation capacity and energy and power density with better cyclic stability in comparison with other nanostructured V_2O_5 cathodes reported recently. [13,56,70–73] The high performance could be ascribed to the nanostructure in this research (Figure 10, inset): the 20–30 nm nanocrystallites provide a shorter diffusion path for Li^+ ion intercalation/deintercalation, and the 10 nm wrinkled gaps offers a higher surface area with more accessible intercalation sites, which favors electrolyte penetration and interface reactions.[19,74] This nanostructure could effectively enhance the phase transition during Li^+ ion intercalation/deintercalation, and it essentially benefits from the presence of V^{4+} serving as the films initiator and catalyst during cathodic deposition, as well as nucleation sites in the annealing process in air. Since a great deal of volumetric change can be accommodated by the nanostructure, the film's mechanical integrity and stability during battery testing is good, resulting in excellent cyclic stability.[75] The external electrical field applied during film deposition helps form a sturdy adhesion to the conductive substrate, which could facilitate better Li^+ ion diffusion and guarantee excellent energy and power density.

3. Conclusions

Nanostructured V_2O_5 thin-film electrodes have been prepared for the first time by cathodic deposition from V_2O_5 and H_2O_2 followed by annealing at 500 °C in air. The mechanisms and reactions for cathodic deposition of V_2O_5 thin films have been discussed in detail: the formation of tetravalent vanadium ions or VO_2 by cathodic deposition initiated and catalyzed the formation and gelation of hydrous vanadium pentoxide films. After annealing the as-deposited $V_2O_{5-x}\cdot nH_2O$ films at 500 °C in air, they show a preferred oriented orthorhombic phase with a crystallite size of 35.1 nm (calculated from XRD patterns). The XPS results show 15% V^{4+} out of V_{total} concentration in the as-deposited $V_2O_{5-x}\cdot nH_2O$ films; all V^{4+} is oxidized to V^{5+} at 500 °C. The "wrinkled" nanostructure of the V_2O_5 films was shown by SEM to be composed of fine nanocrystallites of 20–30 nm size separated by 10 nm gaps. The electrochemistry and phase transitions during Li-ion intercalation and de-intercalation of these cathodic deposited V_2O_5 nanostructured thin films are explicitly discussed in this paper. Electrochemical tests demonstrate that the nanostructured V_2O_5 thin film electrodes possess enhanced phase transition reversibility during Li^+ion intercalation/de-intercalation. The high energy density (900 W h kg^{-1} at 200 mA g^{-1}), power density (28 kW kg^{-1} at 10.5 A g^{-1}), and enhanced phase transitions as well as the good cyclic stability (functioning well in over 200 cycles) can be ascribed to the nanostructure having a higher surface area, shorter Li^+ ion diffusion pathways, and improved mechanical integrity. Cathodic deposited vanadium pentoxide films could become a promising candidate for Li-ion battery cathode materials due to its good electrochemical performance, as well as its simple, flexible, and easily controllable low-cost processing method.

4. Experimental Section

Sample preparation: The films studied in this research were all prepared by cathodic deposition from diluted vanadium pentoxide solutions, which were made according to the procedure reported by Frontenot et al.[36] V_2O_5 powders (99.8%, Alfa-AESAR) were added to de-ionized water and H_2O_2 (30 wt.% in H_2O, Sigma-Aldrich) to form a

solution with a V_2O_5 concentration (C_V) of 0.3 M and $n(H_2O_2)$: $n(V)$ of 8.05 : 1. The resulting solution was stirred for 15 min and sonicated for 15 min respectively while kept in water at a constant temperature for the reactions. It was observed that the yellow slurry started bubbling vigorously and gradually turned orange in color. After 5 min a transparent solution was formed that was ruby red in color. This solution was later diluted to C_v = 0.06 M and then sonicated for 1 h until the solution turned into a brownish red V_2O_5 gel. This gel was further dispersed and diluted to a C_v of 0.0075 M, and stirred in de-ionized water until a brick-red-colored, transparent solution with a pH of 2.6 was formed. This solution was used for cathodic deposition.

For the preparation of V_2O_5 films, fluorine-doped tin oxide (FTO) coated glass was used as the deposition substrate on the negative side, and a Pt plate was used as a counter electrode on the positive side. The distance between the two electrodes was kept constant at 1.5 cm and the deposition voltage was –2.4 V. Deposition was carried out for 3, 5, 10, and 20 min on separate samples to investigate the deposition rate using this method. The films were left in air for one day until completely dried to avoid cracking induced by drastic volume change; the films were then annealed in ambient atmosphere at 500 °C for 3 h followed by a slow cool-down. All samples were stored in vacuum before characterizations and property measurements.

Sample characterization: The thickness of the V_2O_5 films deposited over different times was measured using a Dektak Profilometer 3030 after deposition at room temperature and annealing at 500 °C. The rest of the characterization was conducted on films deposited for 3 min at –2.4 V. Thermogravimetric properties of the V_2O_5 films were investigated by thermogravimetric analysis (TGA 7, PerkinElmer) from room temperature to 600 °C in air at a heating rate of 2 °C min^{-1}. The phase and crystallite size of the V_2O_5 films were studied using X-ray diffraction (XRD, Philips 1820 X-ray diffractometer); the surface morphology and roughness of V_2O_5 films were examined using scanning electron microscopy (SEM, JEOL, JSM-5200) and atomic force microscopy (AFM, Asylum Research MFP-3D). X-Ray photoelectron spectroscopy (XPS) was used to understand and compare the valence status of vanadium in V_2O_5 films before and after annealing and lithium intercalation. All XPS spectra were taken on a Kratos Axis-Ultra DLD spectrometer.

The electrochemical properties of the V_2O_5 thin film electrodes were tested using a standard three-electrode setup with 1 M $LiClO_4$ in propylene carbonate (PC) as electrolyte, a Pt plate as the counter electrode, and Ag/AgCl as the reference electrode. Cyclic voltammetric (CV) curves were measured between 0.6 V–1.8 V (vs. Ag^+/Ag) with scan rate of 5 mV s^{-1}, and the lithium ion intercalation/deintercalation properties and cycling performance were investigated by chronopotentiometric (CP) method in the voltage range of 0.2 V–1.6 V (vs. Ag^+/Ag). Both CV and CP tests were performed using an electrochemical analyzer (CH Instruments, Model 605B).

Supporting Information

Supporting Information is available from the Wiley Online Library or from the author.

Acknowledgements

This research work has been financially supported in part by the National Science Foundation (DMR-0605159 and CMMI- #1030048) and Pacific Northwest National Laboratory (PNNL). The authors would like to thank P. Y. Yang, S. H. Xie, G. Q. Ren, and S. Huang at the University of Washington for the help with Dektak and AFM analysis. Dr. L. Gamble and Dr. J. Hull at Surface Analysis Recharge Center (SARC) at UW are acknowledged for the XPS analysis and thoughtful discussions.

Received: November 20, 2011
Revised: January 11, 2011
Published online: February 2, 2011

[1] G-A. Nazri, G. Pistoia, *Lithium Batteries Science and Technology*, Kluwer Academic, Boston, **2004**.
[2] M. Armand, J.-M. Tarascon, *Nature* **2008**, *451*, 652.
[3] L. F. Nazar, G. Goward, F. Leroux, M. Duncan, H. Huang, T. Kerr, J. Gaubicher, *Int. J. Inorg. Mater.* **2001**, *3*, 191.
[4] M. Hirshes, *Mater. Sci. Eng. B.* **2004**, *108*, 1
[5] A. S. Arico, P. Bruce, B. Scrosati, J.-M. Tarascon, W. V. Schalkwijk, *Nat. Mater.* **2005**, *4*, 366.
[6] Y. Wang, G. Z. Cao, *Adv. Mater.* **2008**, *20*, 2251.
[7] J. Haber, *Catal. Today* **2009**, *142*, 100.
[8] J. S. Im, S. W. Woo, M. J. Jung, Y. S. Lee, *J. Colloid Interface Sci.* **2008**, *327*, 115.
[9] B. Wang, K. Konstantino, D. Wexler, H. Liu, G. X. Wang, *Electrochim. Acta* **2009**, *54*, 4120.
[10] Z. J. Lao, K. Konstantinov, Y. Tournaire, S. H. Hg, G. X. Wang, H. K. Liu, *J. Power Sources* **2006**, *162*, 1451.
[11] J-K. Lee, G-P. Kim, I. K. Song, S-H. Baeck, *Electrochem. Commun.* **2009**, *11*, 1571.
[12] E. Potiron, A. Le, Gal La Salle, A. Verbaere, Y.Piffard, D. Guyomard, *Electrochim. Acta* **1999**, *45*, 197.
[13] Y. Wang, G. Z. Cao, *Electrochim. Acta* **2006**, *51*, 4865.
[14] K. West, B. Zachau-Christiansen, T. Jacobsen, S. Skaarup, *Electrochim. Acta* **1993**, *38*, 1215.
[15] C. Delmas, H. Cognac-Auradou, J. M. Cocciantelli, M. Ménétrier, J. P. Doumerc, *Solid State Ionics* **1994**, *69*, 257.
[16] A-M. Cao, J.-S. Hu, H-P. Liang, L.-J. Wan, *Angew., Chem. Int. Ed.* **2005**, *44*, 4391.
[17] X. Z. Ren, Y. K. Jiang, P. X. Zhang, J. H. Liu, Q. L. Zhang, *J. Sol-Gel Sci. Technol.* **2009**, *51*, 133.
[18] C. M. Ban, N. A. Chernova, M. S. Whittingham, *Electrochem. Commun.* **2009**, *11*, 522.
[19] P. Liu, S-H. Lee, C. E. Tracy, Y. Yan, J. A. Turner, *Adv. Mater.* **2002**, *14*, 27.
[20] M. S. Whittingham, *J. Electrochem. Soc.* **1976**, *123*, 315.
[21] J. D. Jarrell, B. Dolly, J. R. Morgan, *J. Biomed. Mater. Res. A* **2009**, *90A*, 272.
[22] D. M. Yu, S. T. Zhang, D. W. Liu, X. Y. Zhou, S. H. Xie, Q. F. Zhang, Y. Y. Liu, G. Z. Cao, *J. Mater. Chem.* **2010**, *20*, 10841.
[23] C. Delmas, S. Brethes, M. Menetrier, *J. Power Sources* **1991**, *34*, 113.
[24] C. Leger, S. Bach, P. Soundan, J.-P. Pereira, *J. Electrochem. Soc.* **2005**, *152*, A236.
[25] T. Ohzuku, A. Ueda, M. Nagayama, Y. Iwakoshi, H. Komori, *Electrochim. Acta* **1993**, *38*, 1159.
[26] Z. Li, D. Zhang, F. Yang, *J. Mater. Sci.* **2009**, *44*, 2435.
[27] K. Kang, Y. S. Meng, J. Breger, C. P. Grey, G. Ceder, *Science* **2006**, *311*, 977.
[28] A. R. Armstrong, D. W. Tee, F. L. Mantia, P. Novak, P. G. Bruce, *J. Am. Chem. Soc.* **2008**, *130*, 3554.
[29] J. M. Tarascon, D. Guyomard, *Electrochim. Acta* **1993**, *38*, 1221.
[30] G. Pistoia, G. Wang, *Solid State Ionics* **1993**, *66*, 135.
[31] D. M. Yu, C. G. Chen, S. H. Xie, Y. Y. Liu, K. S. Park, X. Y. Zhou, Q. F. Zhang, J. Y. Li, G. Z. Cao, *Energy Environ. Sci.* **2011**in press, DOI: 10.1039/c0ee00313a.
[32] Y-T. Kim, S. Gopukumar, K.-B. Kim, B.-W. Cho, *J. Power Sources* **2003**, *117*, 110.
[33] Y. Y. Zhou, Z. F. Qiu, M. K. Lv, A. Y. Zhang, Q. Ma, *Mater. Lett.* **2007**, *61*, 4073.
[34] C. K. Chan, H. L. Peng, R. D. Twesten, K. Jarausch, X. F. Zhang, Y. Cui, *Nano Lett.* **2002**, *7*, 490.
[35] S. W. Lee, N. Yabuuchi, B. M. Gallan, S. Chen, B-S. Kim, P. T. Hammond, S-H. Yang, *Nat. Nanotechnol.* **2010**, *20*, 1.
[36] C. J. Fontenot, J. W. Wiench, M. Pruski, G. L. Schrader, *J. Phys. Chem. B* **2000**, *104*, 11622.
[37] O. W. Howarth, J. R. Hunt, *J. Chem., Soc., Dalton Trans.* **1979**, *9*, 1388.

[38] A. Butler, M. J. Clague, G. E. Meister, *Chem. Rev.* **1994**, *94*, 625.
[39] B. Alonso, J. Livage, *J. Solid State Chem.* **1999**, *148*, 16.
[40] C. J. Fontenot, J. W. Wiench, M. Pruski, G. L. Schrader, *J. Phys. Chem. B* **2001**, *105*, 10496.
[41] W. M. Latimer, *Oxidation Potenials*, 2nd ed., Prentice-Hall, New York, **1952**
[42] E. Portiron, A. Le Gal La Salle, S. Sarciaux, Y. Piffard, D Guyomard, *J. Power Sources* **1999**, *81–82*, 666.
[43] N. Gharbi, C. Sanchez, J. Livage, J. Lemerle, L. Nejem, J. Lefebvre, *Inorg. Chem.* **1982**, *21*, 2758.
[44] G. A. Pozarnsky, A. V. McCormick, *Chem. Mater.* **1994**, *6*, 380.
[45] G. A. Pozarnsky, A. V. McCormick, *J. Mater. Chem.* **1994**, *4*, 1749.
[46] C. J. Fontenot, J. W. Wiench, G. L. Schrader, M. Prusk, *J. Am. Chem. Soc.* **2002**, *124*, 8435.
[47] R. Rodriguez, *Principles of Polymeric Systems*, John Wiley and Sons, New York, **1988**.
[48] S. I. Liochev, I. Fridovich, *Arch. Biochem. Biophys.* **1991**, *291*, 379.
[49] C. Sanchez, M. Navavi, *Mater. Res. Soc. Symp. Proc.* **1988**, *121*, 93
[50] G. Strukul, *Catalytic oxidations with hydrogen peroxide as oxidant*, Kluwer Academic Pulishers, Dordrecht,The Netherlands, **1991**.
[51] V. Petkov, P. N. Trikalitis, *J. Am. Chem. Soc.* **2002**, *124*, 10157.
[52] J. Livage, *J. Sol-Gel Sci. Technol.* **2000**, *19*, 275.
[53] E. Volz, A. Roosen, W. Hartung, A. Winnacker, *J. Euro. Ceram. Soc.* **2001**, *21*, 2089.
[54] A. Gusev, E. Awakumov, *Sci. Sintering* **2007**, *39*, 51.
[55] G. P. Hollan, F. Huguenin, R. M. Torresi, D. A. Buttry, *J. Electrochem. Soc.* **2003**, *150*, A721.
[56] Y. Wang, H. M. Shang, T. Chou, G. Z. Cao, *J. Phys. Chem. B* **2005**, *109*, 11361.
[57] J. Livage, *Chem. Mater.* **1991**, *3*, 578.
[58] J.-J. Legendre, P. Aldebert, N. Baffier, J. Livage, *J. Colloid Interface Sci.* **1983**, *94*, 84.
[59] S. Beke, L. Korosi, S. Papp, A. Oszko, L. Nanai, *Appl. Surf. Sci.* **2009**, *255*, 9779.
[60] J. Swiatowska-Mrowiecka, V. Maurice, S. Zanna, L. Klein, P. Marcus, *Electrochim. Acta* **2007**, *52*, 5644.
[61] A. Gies, B. Pecquenard, A. Benayad, H. Martinezm D. Gonbeau, H. Fuess, A. Levasseur, *Solid State Ionics* **2005**, *176*, 1627.
[62] D. Alamarguy, J. E. Castle, N. Ibris, A. M. Salvi, *Surf. Interface Anal.* **2006**, *38*, 801.
[63] C. Slebodnick, V. L. Pecoraro, *Inorg. Chim. Acta* **1998**, *283*, 37.
[64] A. M. Salvi, M. R. Guascito, A. DeBonis, F. Simone, A. Pennisi, F. Decker, *Surf. Interface Anal.* **2003**, *35*, 897.
[65] A. Benayad, H. Martinez, A. Gies, B. Pecquenard, A. Levasseur, D. Gonbeau, *J. Phys. Chem. Solids* **2006**, *67*, 1320.
[66] V. M. Mohan, B. Hu, W. L. Qiu, W. Chen, *J. Appl. Electrochem.* **2009**, *39*, 2001.
[67] E. Andrukaitis, *J. Power Sources* **2003**, *119–121*, 205.
[68] P. P. Prosini, Y. Y. Xia, T. Fujieda, R. Vellone, M. Shikano, T. Sakai, *Electrochim. Acta* **2001**, *46*, 2623.
[69] D. L. Liu, S. Y. Zhan, G. Chen, W. C. Pan, C. Z. Wang, Y. J. Wei, *Mater. Lett.* **2008**, *62*, 4210.
[70] D. W. Liu, Y. Y. Liu, B. B. Garcia, Q. F. Zhang, A. Q. Pan, Y-H. Jeong, G. Z. Cao, *J. Mater. Chem.* **2009**, *19*, 8789.
[71] L. Q. Mai, L. Xu, C. H. Han, X. Xu, Y. Z. Luo, S. Y. Zhao, Y. L. Zhao, *Nano Lett.* **2010**, *10*, 4750.
[72] C. M. Ban, N. A. Chernova, M. S. Whittingham, *Electrochem. Commun.* **2009**, *11*, 522.
[73] C. O'Dwyer, V. Lavayen, D. A. Tanner, S. B. Newcomb, E. Benavente, G. Gonzalez, C. M. S. Torres, *Adv. Funct. Mater.* **2009**, *19*, 1736.
[74] Y. Wang, K. Takahashi, K. H. Lee, G. Z. Cao, *J. Phys. Chem. B* **2005**, *109*, 48.
[75] D. W. Liu, B. B. Garcia, Q. F. Zhang, Q. Guo, Y. H. Zhang, S. Sepehri, G. Z. Cao, *Adv. Funct. Mater.* **2009**, *19*, 1015.